Frontiers of Information Technology & Electronic Engineering
www.jzus.zju.edu.cn; engineering.cae.cn; www.springerlink.com
ISSN 2095-9184 (print); ISSN 2095-9230 (online)
E-mail: jzus@zju.edu.cn

An online error calibration method for spaceflight TT&C systems based on LEO-ground DDGPS*

Qiao WANG†, Xiao-jun JIN†‡, Wei ZHANG, Shi-ming MO, Zhao-bin XU, Zhong-he JIN

Micro-Satellite Research Center, Zhejiang University, Hangzhou 310027, China

†E-mail: wqiao2010@zju.edu.cn; axemaster@zju.edu.cn

Received May 19, 2018; Revision accepted Dec. 2, 2018; Crosschecked June 11, 2019

Abstract: To overcome the shortcomings of the traditional measurement error calibration methods for spaceflight telemetry, tracking and command (TT&C) systems, an online error calibration method based on low Earth orbit satellite-to-ground double-differential GPS (LEO-ground DDGPS) is proposed in this study. A fixed-interval smoother combined with a pair of forward and backward adaptive robust Kalman filters (ARKFs) is adopted to solve the LEO-ground baseline, and the ant colony optimization (ACO) algorithm is used to deal with the ambiguity resolution problem. The precise baseline solution of DDGPS is then used as a comparative reference to calibrate the systematic errors in the TT&C measurements, in which the parameters of the range error model are solved by a batch least squares algorithm. To validate the performance of the new online error calibration method, a hardware-in-the-loop simulation platform is constructed with independently developed spaceborne dual-frequency GPS receivers and a Spirent GPS signal generator. The simulation results show that with the fixed-interval smoother, a baseline estimation accuracy (RMS, single axis) of better than 10 cm is achieved. Using this DDGPS solution as the reference, the systematic error of the TT&C ranging system is effectively calibrated, and the residual systematic error is less than 5 cm.

Key words: Spaceflight; low Earth orbit (LEO); Filter; Optimization; Calibration
https://doi.org/10.1631/FITEE.1800308 **CLC number:** TP39; V19

1 Introduction

To ensure the measurement accuracy of spaceflight telemetry, tracking and command (TT&C) systems, the measurement errors (range error, velocity error, and angle error) of spaceflight TT&C systems need to be calibrated. The aim of calibration is to determine and correct the systematic error of the TT&C measurement data, which is affected only by a random error after calibration. At present, traditional calibration methods, including tower calibration and aircraft calibration, are used to calibrate the measurement errors in spaceflight TT&C systems before the spacecraft is launched. The tower calibration method is a static calibration method, which cannot truly reflect the errors characteristic of dynamic systems, and consequently there are limitations in its application. Although aircraft calibration has been widely used, it has shortcomings such as a small dynamic range, long delays, and difficulties in management for flight experiments. The disadvantages of the above traditional calibration methods can be summarized into the following three issues: (1) When calibrated with pre-calibration methods, the residual measurement error is still large; (2) The pre-calibration methods cannot reflect the real error characteristics of on-orbit space missions; (3) The pre-calibration methods cannot cope with the time-

‡ Corresponding author

* Project supported by the National Natural Science Foundation of China (Nos. 60904090 and 61401389), the National Science Foundation for Distinguished Young Scholars of China (No. 61525403), the Joint Fund of the Ministry of Education of China (No. 6141A02033310), and the Fundamental Research Funds for the Central Universities, China (No. 2018QNA4053)

ORCID: Qiao WANG, http://orcid.org/0000-0002-0678-047X; Xiao-jun JIN, http://orcid.org/0000-0002-8804-9890

varying characteristics of measurement errors during the on-orbit operation phase. A large number of on-orbit space missions have shown that the systematic error in the ranging system is still more than 10 m, the velocity error is about 18 cm/s, and the angle error is about 0.14 mrad after calibration (Liu, 2015). Due to the low measurement accuracy of TT&C systems, the determination of satellite orbit precision can reach only 100 m, and the precision of orbit prediction is about 1 km. This level of orbital precision cannot meet the requirements of manned spaceflight, exploration of deep space, or sufficient control in spacecraft rendezvous (Li et al., 2013; Wan et al., 2014). Therefore, TT&C systems now face serious challenges in moving forward. In China, the "Space TT&C Measurement Accuracy Project" has been proposed to improve TT&C measurement accuracy, and the goal of the project is to bring the systematic errors of the ranging systems down to the decimeter level and the velocity errors to the millimeter per second level. Therefore, an online calibration method is necessary to overcome the above disadvantages in traditional calibration methods and ensure TT&C measurement accuracy.

Since the 1960s, the U.S. military has developed several radar calibration satellites. RADCAL and DMSP F-15 (Langer et al., 1994; Martin et al., 2011), launched in 1993 and 1999 respectively, have operated for many years to provide services for radar error calibration. In 2013, the United States Air Force and the University of Hawaii developed the first radar calibration CubeSat, called Ho'oponopono (Martin et al., 2011). To carry out radar error calibration, the zero-difference GPS observations of the CubeSat were used to determine the precise orbit, which served as a comparative reference for radar error calibration. Russia also launched the radar calibration satellite SKRL-7561 in 2013, but its calibration method has not yet been publicly reported. According to the survey results of the existing reports, the satellite-based calibration technique has been widely used in error calibration for ground-based radar equipment, and there are only a few related research reports on the application of satellite-based error calibration methods for China's spaceflight TT&C systems (the universal S-band TT&C system and the spread spectrum TT&C system). A new online error calibration method based on low Earth orbit satellite-to-ground double-differential GPS (LEO-ground DDGPS) is proposed in this study. Using the precise baseline solution of double-differential GPS (DDGPS) as a comparative reference, the measurement error can be precisely calibrated. To the best of the authors' knowledge, this online error calibration method is proposed for the first time. In contrast with the zero-difference GPS-based calibration method, the LEO-ground DDGPS based calibration method has the following advantages: (1) It does not need to know the accurate coordinates of the ground stations; (2) DDGPS observations can eliminate the influence of the navigation satellite clock error and the receiver clock error; (3) If the GPS phase ambiguity is fixed, the precise LEO-ground baseline solution can be achieved (Švehla and Rothacher, 2003).

Compared with the terrestrial differential GPS systems (Takasu and Yasuda, 2008, 2009; Lin, 2015; Matias et al., 2015), the design of the estimation algorithm for the LEO-ground DDGPS system is more challenging due to the high dynamics and large baseline length. With the conventional extended Kalman filter (EKF), it is difficult for the baseline solution to converge to high accuracy quickly because of fewer common-view GPS satellites, short common-view arcs, and poor GPS geometry. To solve this problem, a fixed-interval smoother (Gelb, 1974; Liu et al., 2010) combined with a pair of forward and backward adaptive robust Kalman filters (ARKFs) is adopted to solve the LEO-ground baseline, and a cascading integer resolution method (Blewitt, 1989; Teunissen et al., 2003) based on the ant colony optimization (ACO) algorithm (Socha and Dorigo, 2008) is used to solve the ambiguity resolution problem. In contrast to the classical least-squares ambiguity decorrelation algorithm (LAMDA) (Teunissen et al., 1997; Verhagen et al., 2013), which transfers the original integer least-squares problem to a new one by means of the so-called *Z*-transformations before the stage of searching for the optimal estimates, the ACO algorithm searches for the optimal integer estimates in a straightforward manner without decorrelation of ambiguity.

2 Online error calibration method

ZDPS-3, the 3rd generation nano-satellite that was designed and manufactured by the Micro-

Satellite Research Center of Zhejiang University, is used to provide online services for error calibration of the spaceflight TT&C systems. It is equipped with a spaceborne dual-frequency GPS receiver, an S-band transponder, a C-band transponder, and other cooperative payloads (Fig. 1).

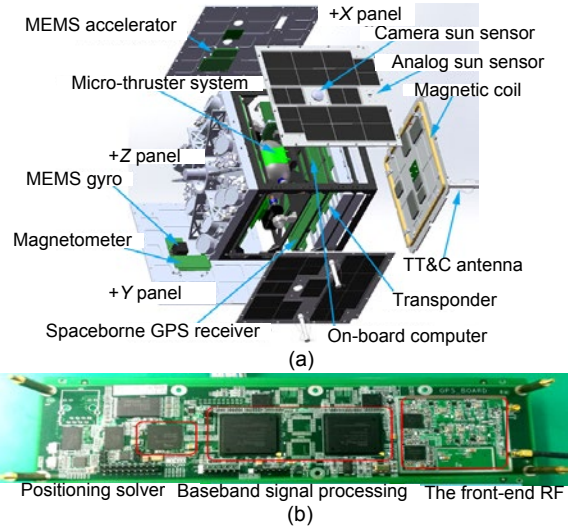

Fig. 1 Calibration satellite: (a) ZDPS-3; (b) spaceborne GPS receiver

Spaceborne GPS observations are downloaded to the ground via the LEO-ground S-band communication link. The LEO-ground DDGPS system was constructed based on spaceborne GPS observations and ground station GPS observations. The systematic error calibration procedure for TT&C measurements can be divided into three steps:

1. The spaceflight TT&C system tracks the space cooperative objects to obtain measurement data.

2. The LEO-ground baseline solution is solved based on DDGPS observations.

3. The baseline solution is then used as a comparative reference to solve the TT&C measurement error model.

In the following part, the algorithm for the baseline solution and the solver of the measurement error model are described in detail.

2.1 Algorithm for the LEO-ground baseline solution

A precise LEO-ground baseline solution is the basis of the online error calibration method. The baseline solutions, estimated by a pair of forward and backward ARKFs, are smoothed by a fixed-interval smoother. The key issues for the LEO-ground baseline solution algorithm are described in this subsection.

2.1.1 Observation model

The double-differential (DD) ionosphere-free linear combination of the pseudorange and carrier phase (Xu and Xu, 2016) is expressed as Eqs. (1)–(4). The tropospheric delay of the ground GPS observation cannot be eliminated by DDGPS, and it needs to be treated as an estimated parameter of the ARKF filter.

$$P_{\mathrm{IF,rb}}^{jk}=\rho_{\mathrm{rb}}^{jk}-(T_{\mathrm{b}}^{j}-T_{\mathrm{b}}^{k})+\varepsilon_{\mathrm{rb},P}^{jk}, \tag{1}$$

$$\Phi_{\mathrm{IF,rb}}^{jk}=\rho_{\mathrm{rb}}^{jk}-(T_{\mathrm{b}}^{j}-T_{\mathrm{b}}^{k})+(B_{\mathrm{IF,rb}}^{j}-B_{\mathrm{IF,rb}}^{k})+\varepsilon_{\mathrm{IF},\Phi}^{jk}, \tag{2}$$

$$B_{\mathrm{IF,rb}}^{j}=B_{\mathrm{IF,r}}^{j}-B_{\mathrm{IF,b}}^{j},\ B_{\mathrm{IF,rb}}^{k}=B_{\mathrm{IF,r}}^{k}-B_{\mathrm{IF,b}}^{k}, \tag{3}$$

$$\begin{cases}B_{\mathrm{IF}}^{j}=\dfrac{f_1^2}{f_1^2-f_2^2}\lambda_1N_1^{j}-\dfrac{f_2^2}{f_1^2-f_2^2}\lambda_2N_2^{j},\\ B_{\mathrm{IF}}^{k}=\dfrac{f_1^2}{f_1^2-f_2^2}\lambda_1N_1^{k}-\dfrac{f_2^2}{f_1^2-f_2^2}\lambda_2N_2^{k},\end{cases} \tag{4}$$

where P and Φ are GPS pseudorange and carrier phase measurement (m) respectively, T is the tropospheric delay (m), B is the carrier phase bias (m), superscripts j and k are the GPS pseudorandom noise (PRN) number, subscripts r and b denote the rover and base station respectively, subscript IF denotes ionosphere-free linear combination, which is used to eliminate the ionosphere delay, λ_1 and λ_2 are GPS L_1/L_2 carrier length (m), f_1 and f_2 are GPS L_1/L_2 carrier frequency (Hz), and N_1 and N_2 are GPS L_1/L_2 phase ambiguity (cycle).

The tropospheric delay model in the line-of-sight direction can be written in the form of Eq. (6), where the tropospheric zenith hydrostatic delay $Z_{\mathrm{H,b}}$ is given by the Saastamoinen model (Saastamoinen, 1972) and its hydrostatic mapping function $m_{\mathrm{H}}(\mathrm{El}_{\mathrm{b}}^{\mathrm{s}})$, which employs the Niell mapping function (NMF) model (Niell, 1996; Boehm et al., 2006). The tropospheric zenith wet delay is expressed as the difference between the tropospheric zenith total delay $Z_{\mathrm{T,b}}$ and tropospheric zenith hydrostatic delay $Z_{\mathrm{H,b}}$. The factor $m(\mathrm{El}_{\mathrm{b}}^{\mathrm{s}})$ is defined as Eq. (5), where the wet mapping function $m_{\mathrm{W}}(\mathrm{El}_{\mathrm{b}}^{\mathrm{s}})$ also employs the NMF model. The

zenith total delay $Z_{\mathrm{T,b}}$ and the gradient parameters ($G_{\mathrm{N,b}}$, $G_{\mathrm{E,b}}$) are estimated as unknown parameters to absorb the influence of the tropospheric delay on the baseline solution.

$$m(\mathrm{El}_{\mathrm{b}}^{\mathrm{s}}) = m_{\mathrm{W}}(\mathrm{El}_{\mathrm{b}}^{\mathrm{s}})\Big[1+\cot(\mathrm{El}_{\mathrm{b}}^{\mathrm{s}})(G_{\mathrm{N,b}}\cos(\mathrm{Az}_{\mathrm{b}}^{\mathrm{s}}) +G_{\mathrm{E,b}}\sin(\mathrm{Az}_{\mathrm{b}}^{\mathrm{s}}))\Big], \tag{5}$$

$$T_{\mathrm{b}}^{\mathrm{s}} = m_{\mathrm{H}}(\mathrm{El}_{\mathrm{b}}^{\mathrm{s}})Z_{\mathrm{H,b}} + m(\mathrm{El}_{\mathrm{b}}^{\mathrm{s}})(Z_{\mathrm{T,b}} - Z_{\mathrm{H,b}}), \tag{6}$$

where $m_{\mathrm{W}}(\mathrm{El})$ is the wet mapping function, $G_{\mathrm{N,b}}$ and $G_{\mathrm{E,b}}$ are north and east gradient parameters respectively, $Z_{\mathrm{T,b}}$ is the tropospheric zenith total delay (m), $Z_{\mathrm{H,b}}$ is the tropospheric zenith hydro-static delay (m), and $m_{\mathrm{H}}(\mathrm{El})$ is the hydro-static mapping function.

In parameter estimation, the state vector of the DDGPS system is defined as

$$\boldsymbol{X} = (\Delta r,\ \Delta v,\ Z_{\mathrm{b}},\ G_{\mathrm{N,b}},\ G_{\mathrm{E,b}},\ B_{\mathrm{LC,rb}}^{\mathrm{i}}), \tag{7}$$

where Δr and Δv denote the relative position and velocity of the LEO-ground baseline respectively. $B_{\mathrm{LC,rb}}^{\mathrm{i}}$ is the single-difference (SD) ionosphere-free linear combination of the carrier phase bias (m). The ARKF filter uses the SD ionosphere-free linear combination of the carrier phase bias instead of DD to avoid hand-over handling of reference satellites.

The ARKF filter uses the DD ionosphere-free linear combination as the observation model, and the state vector (Δr, Δv) of the ARKF filter is updated by a relatively reduced dynamic model.

2.1.2 ARKF filter

The ARKF filter (Yang and Gao, 2006) has been successfully applied in positioning and navigation, because it can optimize the system output by tuning the covariance parameters of process noise $\boldsymbol{Q}$ and observation noise $\boldsymbol{R}$. The ARKF filter is expressed as the following equations:

$$\hat{\boldsymbol{X}}_{k,k-1} = \boldsymbol{\Phi}_{k,k-1}\hat{\boldsymbol{X}}_{k-1}, \tag{8}$$

$$\boldsymbol{P}_{k,k-1} = \boldsymbol{\Phi}_{k,k-1}\boldsymbol{P}_{k-1}\boldsymbol{\Phi}_{k,k-1}^{\mathrm{T}} + \boldsymbol{\Gamma}_{k-1}\boldsymbol{Q}_{k-1}\boldsymbol{\Gamma}_{k-1}^{\mathrm{T}}, \tag{9}$$

$$\boldsymbol{K}_k = \frac{1}{\alpha_k}\boldsymbol{P}_{k,k-1}\boldsymbol{H}_k^{\mathrm{T}}\left(\frac{1}{\alpha_k}\boldsymbol{H}_k\boldsymbol{P}_{k,k-1}\boldsymbol{H}_k^{\mathrm{T}} + \bar{\boldsymbol{R}}_k\right)^{-1}, \tag{10}$$

$$\hat{\boldsymbol{X}}_k = \hat{\boldsymbol{X}}_{k,k-1} + \boldsymbol{K}_k(\boldsymbol{L}_k - \boldsymbol{H}_k\hat{\boldsymbol{X}}_{k,k-1}), \tag{11}$$

$$\boldsymbol{P}_k = (\boldsymbol{I} - \boldsymbol{K}_k\boldsymbol{H}_k)\boldsymbol{P}_{k,k-1}(\boldsymbol{I} - \boldsymbol{K}_k\boldsymbol{H}_k)^{\mathrm{T}} + \boldsymbol{K}_k\bar{\boldsymbol{R}}_k\boldsymbol{K}_k^{\mathrm{T}}, \tag{12}$$

where subscripts k and $k-1$ denote the current time and the previous time respectively, $\boldsymbol{\Phi}_{k,k-1}$ is the state transition matrix, $\hat{\boldsymbol{X}}_{k,k-1}$ and $\boldsymbol{P}_{k,k-1}$ denote the state estimation and the covariance matrix at previous time $k-1$ respectively, $\boldsymbol{\Gamma}$ is the system noise driven matrix, α_k is the adaptive factor, $\boldsymbol{K}$ is the gain matrix, $\boldsymbol{L}$ is the observation vector, $\boldsymbol{H}$ is the design matrix, $\hat{\boldsymbol{X}}_k$ and $\boldsymbol{P}_k$ denote the state estimation and the covariance matrix at current time k respectively, $\boldsymbol{I}$ is the identify matrix, and $\bar{\boldsymbol{R}}_k$ is the equivalent covariance matrix.

The adaptive factor α_k is used to tune the weights of the predictions, and the equivalent covariance matrix $\bar{\boldsymbol{R}}_k$ is used to balance the contribution of GPS observations.

1. Adaptive factor

The prior error $\bar{V}_k$ in the process of the ARKF filter is called the innovation vector (Yang et al., 2006), which is given as Eq. (13). According to the law of error propagation, the covariance matrix $\boldsymbol{P}_{\bar{V}}$ of the innovation vector is formed as Eq. (14). The estimation covariance matrix of the innovation can be obtained by Eq. (15). Then the adaptive factor α_k is given as Eq. (16).

$$\bar{\boldsymbol{V}}_k = \boldsymbol{L}_k - \boldsymbol{H}_k\hat{\boldsymbol{X}}_{k,k-1}, \tag{13}$$

$$\boldsymbol{P}_{\bar{V}} = \boldsymbol{H}_k\boldsymbol{P}_{k,k-1}\boldsymbol{H}_k^{\mathrm{T}} + \bar{\boldsymbol{R}}_k, \tag{14}$$

$$\hat{\boldsymbol{P}}_{\bar{V}} = \bar{\boldsymbol{V}}_k\bar{\boldsymbol{V}}_k^{\mathrm{T}}, \tag{15}$$

$$\alpha_k \approx \begin{cases} \mathrm{tr}(\boldsymbol{P}_{\bar{V}})/\mathrm{tr}(\hat{\boldsymbol{P}}_{\bar{V}}), & \mathrm{tr}(\hat{\boldsymbol{P}}_{\bar{V}}) > \mathrm{tr}(\boldsymbol{P}_{\bar{V}}), \\ 1, & \text{otherwise.} \end{cases} \tag{16}$$

When $\alpha_k<1$, the weight of the prediction states can be reduced.

2. Equivalent covariance matrix

In traditional positioning and navigation algorithms, the observation is discarded when the observation noise is large. In this subsection, the quality control for GPS observations is constructed using the equivalent covariance matrix $\bar{\boldsymbol{R}}_k$.

$\bar{\boldsymbol{R}}_k$ is obtained based on the posterior residual error $\boldsymbol{V}_k$ as shown in Eq. (17). The standardized residual $\tilde{\boldsymbol{V}}_{k,(i)}$ is given by Eq. (18), where E and D

denote the expectation and variance of the posterior residual error $\boldsymbol{V}_k$, respectively.

$$\boldsymbol{V}_k = \boldsymbol{L}_k - \boldsymbol{H}_k \hat{\boldsymbol{X}}_k, \tag{17}$$

$$\tilde{V}_{k,(i)} = \frac{\left|\boldsymbol{V}_i - E(\boldsymbol{V}_k)\right|}{D(\boldsymbol{V}_k)}. \tag{18}$$

The diagonal elements of $\bar{\boldsymbol{R}}_k$ are recorded as $\bar{R}_{k,(i,i)}$, and $\bar{R}_{k,(i,j)}$ denotes the non-diagonal elements. According to the IGG-III scheme (Yang and Gao, 2006), $\bar{R}_{k,(i,i)}$ is expressed as

$$\bar{R}_{k,(i,i)} = \begin{cases} R_{k,(i,i)}, & \left|\tilde{V}_{k,(i)}\right| < k_0, \\ R_{k,(i,i)} \dfrac{\left|\tilde{V}_{k,(i)}\right|}{k_0} \left(\dfrac{k_1 - k_0}{k_1 - \left|\tilde{V}_{k,(i)}\right|} \right)^2, & k_0 \le \left|\tilde{V}_{k,(i)}\right| \le k_1, \\ 10^8 R_{k,(i,i)}, & \left|\tilde{V}_{k,(i)}\right| > k_1, \end{cases} \tag{19}$$

where k_0 and k_1 are the threshold values of the standardized residual $\tilde{V}_{k,(i)}$, in the ranges of 1.0–1.5 and 3.0–5.0, respectively, and $R_{k,(i,i)}$ are the diagonal elements of observation noise $\boldsymbol{R}_k$.

The non-diagonal elements $\bar{R}_{k,(i,j)}$ are given by

$$\bar{R}_{k,(i,j)} = \frac{R_{k,(i,j)}}{\sqrt{R_{k,(i,i)} R_{k,(j,j)}}} \bar{R}_{k,(i,i)} \bar{R}_{k,(j,j)}, \tag{20}$$

where $R_{k,(i,j)}$ are the non-diagonal elements of $\boldsymbol{R}_k$.

The above formulas indicate that the equivalent covariance matrix $\bar{\boldsymbol{R}}_k$ can be used to tune the weight of GPS observations.

2.1.3 Carrier phase ambiguity resolution

The carrier phase ambiguity resolution is the key step to obtain a precise baseline solution. The cascading integer resolution method based on the ACO algorithm is adopted to fix the integer ambiguity. The ambiguity fixing procedure is described as follows:

$$N_{1,\mathrm{rb}}^{jk} = \left(B_{\mathrm{IF,rb}}^{jk} - f_2^2 \lambda_2 N_{\mathrm{w,rb}}^{jk} / (f_1^2 - f_2^2) \right) / \lambda_c, \tag{21}$$

$$\lambda_c = c / (f_1 + f_2), \tag{22}$$

$$B_{\mathrm{IF,rb}}^{jk} = B_{\mathrm{IF,rb}}^{j} - B_{\mathrm{IF,rb}}^{k}, \tag{23}$$

$$N_{\mathrm{w,rb}}^{jk} = N_{1,\mathrm{rb}}^{jk} - N_{2,\mathrm{rb}}^{jk}, \tag{24}$$

$$v = \left(\frac{f_1^2}{f_1^2 - f_2^2} \lambda_1 N_{1,\mathrm{rb}}^{jk} - \frac{f_2^2}{f_1^2 - f_2^2} \lambda_2 N_{2,\mathrm{rb}}^{jk} \right) - B_{\mathrm{IF,rb}}^{jk}. \tag{25}$$

1. Wide-lane ambiguity resolution

The Melbourne–Wübbena linear combination of GPS observations (Xu and Xu, 2006) is used to solve the float solution of the DD wide-lane ambiguity $N_{\mathrm{w,rb}}^{jk}$. Then, $N_{\mathrm{w,rb}}^{jk}$ is fixed by rounding the float ambiguity solution and validating the covariance of the float solution.

2. Narrow-lane ambiguity resolution

$B_{\mathrm{IF,rb}}^{jk}$ denotes the DD ionosphere-free phase bias, which can be obtained from the ARKF states $B_{\mathrm{IF,rb}}^{j}$ and $B_{\mathrm{IF,rb}}^{k}$ as shown in Eq. (23). If ($N_{\mathrm{w,rb}}^{jk}$, $B_{\mathrm{IF,rb}}^{jk}$) are resolved, the float solution of DD phase ambiguity on carrier L_1/L_2 ($N_{1,\mathrm{rb}}^{jk}$, $N_{2,\mathrm{rb}}^{jk}$) is obtained according to Eqs. (21)–(24). To improve the baseline accuracy, the float narrow-lane ambiguities are resolved into integer values by the ACO algorithm.

Algorithm 1 ACO algorithm

Input: maximum number of iterations: imax;
number of ants: nant;
dimensionality of the ambiguity: *n*;
loop count: cnt=0.
initialize the solution archive
while the stop condition is not met and cnt<imax **do**
  for *a*=1 to nant **do**
    for *i*=1 to *n* **do**
      ant based solution construction
    end for
  end for
  pheromone update (update solution archive)
  cnt++
end while
Output: best solution.

The ACO algorithm is often applied to the traveling salesman problem (Dorigo et al., 1996), vehicle routing problems (Reimann et al., 2004), and many other combinatorial optimization problems. Here, the ACO algorithm is adopted to solve the ambiguity resolution problem. Algorithm 1 gives a pseudo-code description of the ACO algorithm. The ambiguity

resolution process of the ACO algorithm consists of two stages. The first stage is the so-called ant-based solution construction (Socha and Dorigo, 2008; Jazaeri et al., 2013), and the second is pheromone update.

(1) Ant-based solution construction

The float narrow-lane ambiguities $\boldsymbol{N}$ and their covariance matrix $\boldsymbol{Q}_{\boldsymbol{N}}$ can be acquired when wide-lane ambiguity is fixed. The most appropriate integer vector $\hat{\boldsymbol{N}}$ for the float narrow-lane ambiguities $\boldsymbol{N}$ is obtained by solving an integer least-squares problem expressed as

$$\min\left((\boldsymbol{N}-\hat{\boldsymbol{N}})^{\mathrm{T}}\boldsymbol{Q}_{\boldsymbol{N}}{}^{-1}(\boldsymbol{N}-\hat{\boldsymbol{N}})\right). \tag{26}$$

The ACO algorithm tracks a number of integer vectors $\hat{\boldsymbol{N}}$ and stores them in a solution archive T (Table 1). In Table 1, S_l denotes the l^{th} solution ($\hat{N}_1^l$, $\hat{N}_2^l$, …, $\hat{N}_n^l$) of the ambiguity. The i^{th} ambiguity of the l^{th} solution is hereby denoted by $\hat{N}_i^l$. ($\hat{N}_i^1$, $\hat{N}_i^2$, …, $\hat{N}_i^k$) is the alternation of the i^{th} ambiguity. The size of the solution archive is set to k. The objective function f is expressed as Eq. (27). The solutions of $\hat{\boldsymbol{N}}$ in the archive are ordered according to their quality as shown in Eq. (28), so S_1 is the best integer ambiguity solution.

$$f=(\boldsymbol{N}-\hat{\boldsymbol{N}}_i)^{\mathrm{T}}\boldsymbol{Q}_{\boldsymbol{N}}^{-1}(\boldsymbol{N}-\hat{\boldsymbol{N}}_i), \tag{27}$$

$$f(S_1)\le f(S_2)\le\ldots\le f(S_l)\le\ldots\le f(S_k). \tag{28}$$

Table 1 Integer vector $\hat{\boldsymbol{N}}$ in a solution archive T

Solution archive						
S_1	$\hat{N}_1^1$	…	$\hat{N}_i^1$	…	$\hat{N}_n^1$	$f(S_1)$
S_2	$\hat{N}_1^2$	…	$\hat{N}_i^2$	…	$\hat{N}_n^2$	$f(S_2)$
⋮	⋮	…	⋮	…	⋮	⋮
S_l	$\hat{N}_1^l$	…	$\hat{N}_i^l$	…	$\hat{N}_n^l$	$f(S_l)$
⋮	⋮	…	⋮	…	⋮	⋮
S_k	$\hat{N}_1^k$	…	$\hat{N}_i^k$	…	$\hat{N}_n^k$	$f(S_k)$

The GPS carrier observation noise usually obeys Gaussian distribution (Xu and Xu, 2016), so the i^{th} carrier ambiguity $\hat{N}_i$ can be generated by sampling the Gaussian distribution G_i as shown in Eq. (29). This can be done using a uniform random generator in conjunction with the Box–Muller method (Box and Muller, 1958). The mean u_i and the standard deviation δ_i of G_i are given as Eqs. (30) and (31) according to the previously stored solution archive. The mean u_i is taken as the first solution of the i^{th} ambiguity to ensure the evolution of the ambiguity to the optimal solution. The standard deviation δ_i reflects the dispersion of the i^{th} ambiguity ($\hat{N}_i^1$, $\hat{N}_i^2$, …, $\hat{N}_i^k$). In a new iteration, the new i^{th} ambiguity denoted as $\hat{N}_{i,\text{new}}$ is generated by sampling the Gaussian distribution, and then rounded to the nearest integer as shown in Eq. (32).

$$G_i=\frac{1}{\sqrt{2\pi}\delta_i}\exp\left(-\frac{(x-u_i)^2}{2\delta_i^2}\right), \tag{29}$$

$$u_i=\hat{N}_i^1, \tag{30}$$

$$\delta_i=\frac{1}{k-1}\sum_{l=1}^{k}\left|\hat{N}_i^l-\hat{N}_i^1\right|, \tag{31}$$

$$\hat{N}_{i,\text{new}}=\text{floor}(\hat{N}_{i,\text{new}}+0.5). \tag{32}$$

In this way, a new ambiguity solution can be acquired per ant, per iteration. The optimal ambiguity solution can be obtained after numerical iterations.

(2) Pheromone update

When all ants get their newly generated solutions, the solution archive is updated by removing the worst solutions and adding the new best solutions according to the objective function f. The total size of the archive does not change and the solutions in the archive are sorted by their quality. This procedure ensures that the best solutions are stored in the archive.

3. Feedback

Once ($N_{1,\text{rb}}^{jk}$, $B_{2,\text{rb}}^{jk}$) have been fixed, a new residual v as given in Eq. (25) is constructed and then used as a feedback to update the ARKF states.

2.1.4 Fixed-interval smoother

As a post-processing method, the fixed-interval smoother is used to smooth the baseline solution of the forward and backward ARKFs. The processing procedure of the fixed-interval smoother is described as follows:

1. Forward filter

Using the forward ARKF filter, the state vector $\hat{\boldsymbol{x}}_k^{\mathrm{F}}$ and covariance matrix $\boldsymbol{P}_k^{\mathrm{F}}$ are solved and then stored.

2. Backward filter

Using the backward ARKF filter, the state vector $\hat{\boldsymbol{x}}_k^{\mathrm{B}}$ and covariance matrix $\boldsymbol{P}_k^{\mathrm{B}}$ are solved and then stored.

3. Weighted combination

$$\boldsymbol{P}_k^{\mathrm{S}}=\left((\boldsymbol{P}_k^{\mathrm{F}})^{-1}+(\boldsymbol{P}_k^{\mathrm{B}})^{-1}\right)^{-1}, \tag{33}$$

$$\boldsymbol{x}_k^{\mathrm{S}}=\boldsymbol{P}_k^{\mathrm{S}}\left((\boldsymbol{P}_k^{\mathrm{F}})^{-1}\boldsymbol{x}_k^{\mathrm{F}}+(\boldsymbol{P}_k^{\mathrm{B}})^{-1}\boldsymbol{x}_k^{\mathrm{B}}\right). \tag{34}$$

In the fixed-interval smoother as shown in Eqs. (33) and (34), $\boldsymbol{x}_k^{\mathrm{S}}$ denotes the smoothed state vector and $\boldsymbol{P}_k^{\mathrm{S}}$ is the smoothed covariance matrix.

2.2 Error calibration for TT&C systems

Spaceflight TT&C systems track low Earth orbit satellites (LEOs) to obtain range, velocity, angle, and conduct other measurements. Although in this study only range error calibration is discussed, the relevant principles are also applicable to error calibration in velocity and angle measurements.

The flowchart for the error calibration procedure is shown in Fig. 2. First, the LEO-ground distance value $R_{\mathrm{DGPS},\,i}$, which is used as a comparative reference for error calibration, is obtained by converting the DDGPS baseline vector Δr into a scalar, which should be modified with the inter-system bias. The inter-system bias includes the time synchronization error, the antenna phase center offset between the GPS receiver and the TT&C system, etc. Meanwhile, the range error model is set up and the range measurement $R_{\mathrm{TT\&C},i}$ is obtained. Second, the range error ΔR_i of the TT&C system is obtained as Eq. (35). Finally, the range error model is solved with a batch least-squares (LSQ) algorithm.

$$\Delta R_i=R_{\mathrm{DGPS},i}-R_{\mathrm{TT\&C},i}. \tag{35}$$

2.2.1 Range error model of the TT&C system

The range error model of the TT&C system can be expressed as

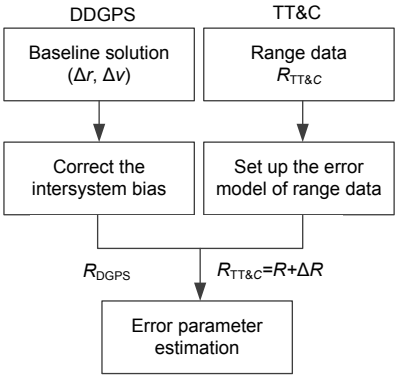

Fig. 2 Flowchart of the error calibration procedure

$$\Delta R=R\left(\frac{\Delta c}{c}-\frac{\Delta f}{f}\right)+\frac{c}{4\pi f}\Delta\phi, \tag{36}$$

where ΔR is the range error and R is the distance from the ground station to the LEO. c and Δc are the light velocity and the light velocity uncertain error respectively. f and Δf are the frequency and the frequency error of the TT&C system respectively. $\Delta\phi$ is the phase measurement error, which includes mainly zero error, zero drift error, tropospheric delay, and ionospheric delay. The range error model can be derived as

$$\begin{aligned}\Delta R=&\,a_{\mathrm{f}}R+\Delta R_{\mathrm{g0}}+a_{\mathrm{g0}}\Delta t+\Delta R_{\mathrm{s0}}\\&+a_{\mathrm{s0}}\Delta t+R_{\mathrm{trop}}+R_{\mathrm{ion}}+\varepsilon,\end{aligned} \tag{37}$$

where Δt is the travel time, $a_{\mathrm{f}}R$ includes the light velocity uncertain error and the frequency error, ΔR_{g0} and $a_{\mathrm{g0}}\Delta t$ are zero error and zero drift error of a ground station respectively, ΔR_{s0} and $a_{\mathrm{s0}}\Delta t$ are zero error and zero drift error of a LEO respectively, a_{f}, a_{g0}, and a_{s0} are error parameters, R_{trop} is the tropospheric delay, R_{ion} is the ionospheric delay, and ε is a random error.

To simplify the error calibration procedure, the tropospheric delay and ionospheric delay are defined as the following:

$$\begin{cases}R_{\mathrm{trop}}=R_{\mathrm{trop,model}}+\mathrm{res}_{\mathrm{trop}},\\ \mathrm{res}_{\mathrm{trop}}=a_{\mathrm{trop}}/\sin\mathrm{El}_{\mathrm{r}}^{s_i},\\ R_{\mathrm{ion}}=R_{\mathrm{ion,model}}+\mathrm{res}_{\mathrm{ion}},\\ \mathrm{res}_{\mathrm{ion}}=5\times10^{-9}a_{\mathrm{ion}}/\sin\mathrm{El}_{\mathrm{r}}^{s_i},\end{cases} \tag{38}$$

where $R_{\text{trop,model}}$ is the tropospheric delay corrected by a model, res_{trop} is the residual tropospheric delay, a_{trop} is the error parameter of tropospheric delay, $\text{El}_{\text{r}}^{s_i}$ is the elevation angle in the line of sight from a ground station to a LEO, $R_{\text{ion,model}}$ is the ionospheric delay corrected by a model, res_{ion} is the residual ionospheric delay, and a_{ion} is the error parameter of ionospheric delay.

The tropospheric delay in the line-of-sight from the ground station to the LEO is corrected by the classical Saastamoinen model. Then the residual tropospheric delay can be formed as a function of $\text{El}_{\text{r}}^{s_i}$. Similarly, the ionospheric delay is corrected using a simple broadcast model (Zhang et al., 2006). Then, the residual ionospheric delay can be simply defined as $5\times10^{-9}a_{\text{ion}}/\sin\text{El}_{\text{r}}^{s_i}$.

2.2.2 Solver of the range error model

The range error model is solved by a batch LSQ algorithm. Assume the range errors ΔR_i are given and they can be modeled as the following linear Eqs. (39) and (40) of an unknown parameter $\boldsymbol{x}_R$ and a random error $\boldsymbol{v}_R$. $\boldsymbol{H}_i$ in Eq. (40) denotes the design matrix.

$$\boldsymbol{x}_R=(a_{\text{f}},\ \Delta R_{\text{g0}},\ a_{\text{g0}},\ \Delta R_{\text{s0}},\ a_{\text{s0}},\ a_{\text{trop}},\ a_{\text{ion}}), \quad (39)$$

$$\Delta\boldsymbol{R}_i=\boldsymbol{H}_i\boldsymbol{x}_R+\boldsymbol{v}_R. \quad (40)$$

3 Hardware-in-the-loop simulation

To test and validate the online error calibration method, a hardware-in-the-loop simulation platform is constructed. As shown in Fig. 3, the simulation platform comprises a Spirent 9000 GPS signal generator and a pair of GPS receivers. Assume that two LEOs operate on the same orbital plane and that two ground stations track the satellites. The scenario for the signal generator is set according to Tables 2 and 3, where SPACEA and SPACEB are two LEOs, and GA and GB are the ground stations.

3.1 Baseline solution of DDGPS

The LEO-ground DDGPS system is formed based on the condition where the LEO and the ground stations have more than seven common-view GPS satellites to guarantee the baseline accuracy. Thus, three LEO-ground baselines SPACEA to GA, SPACEA to GB, and SPACEB to GB, recorded as B1, B2, and B3 respectively, are selected for simulation (Table 4). A pair of forward and backward ARKFs are adopted to calculate the LEO-ground baseline solution, and then the baseline solution of the two filters is smoothed with a fixed-interval smoother.

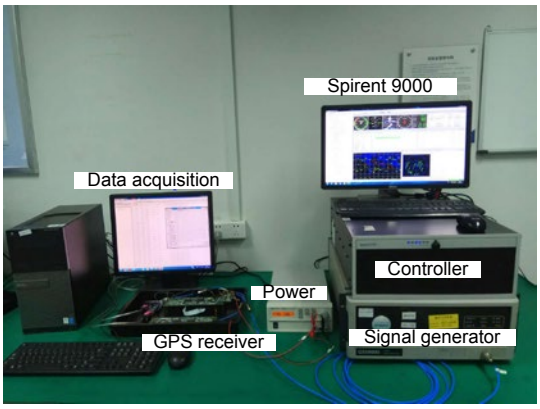

Fig. 3 Hardware-in-the-loop simulation setup

Table 2 Orbital element of the LEOs

Orbital element	SPACEA	SPACEB
a	6 907 395.5 m	6 907 395.5 m
e	0.001 163	0.001 163
i	97.4304°	97.4304°
Ω	−64.4389°	−64.4389°
ω	128.1038°	128.1038°
M	76.7532°	84.7532°

Table 3 Position of the ground stations

Ground station	Position* (m)
GA	(3 248 360.0744, −2 145 154.0945, −5 035 533.2523)
GB	(−5 115 381.9539, 3 528 865.6377, 1 430 801.2013)

* Earth-centered Earth-fixed (ECEF) coordinates

Table 4 Three LEO-ground baselines

Item	Time span
B1	2016/02/08 03:05:30–2016/02/08 03:28:30
B2	2016/02/08 03:41:00–2016/02/08 04:04:30
B3	2016/02/08 00:29:00–2016/02/08 01:02:30

The results of the three smoothed baseline solutions are shown in Figs. 4–6. As shown in Table 5, with the fixed-interval smoother, a baseline accuracy (RMS, single axis) of better than 10 cm is achieved.

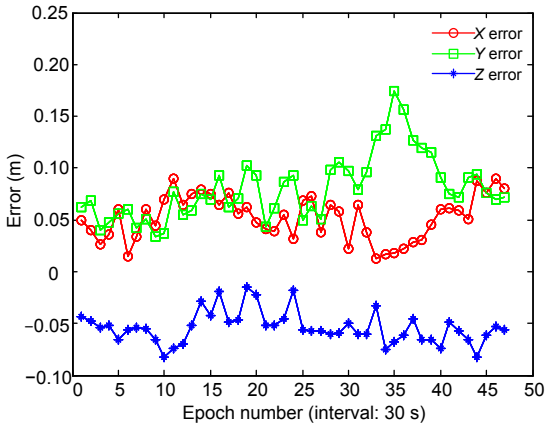

Fig. 4 Solution error of baseline B1

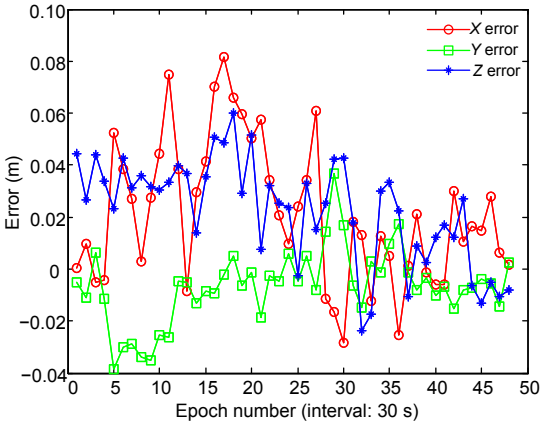

Fig. 5 Solution error of baseline B2

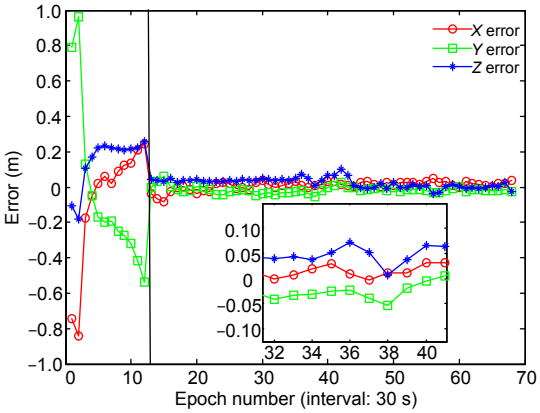

Fig. 6 Solution error of baseline B3

Within the period of time for the simulation, the baseline solutions B1 and B2, shown in Figs. 4 and 5, are at the centimeter level. However, the baseline solution B3 needs 13 epochs to converge to the centimeter level, and the vertical dotted line represents the convergence time in Fig. 6. The convergence of the baseline solution is affected by the geometric configuration of the observed GPS satellites and the observation noise of the GPS receivers. Furthermore, the convergence speed of the error calibration procedure is determined mainly by the convergence of the baseline solution.

Table 5 The smoothed baseline accuracy and the fixing probability of carrier phase ambiguity

Item	Value		
	B1	B2	B3
x-axis (RMS, m)	0.057	0.033	0.025
y-axis (RMS, m)	0.094	0.015	0.024
z-axis (RMS, m)	0.054	0.030	0.036
|baseline| (RMS, m)	0.120	0.047	0.050
NW	57%	55%	48%
N_1	30%	32%	36%

As shown in Table 5, the fixing probability of the wide-lane carrier phase ambiguity NW is about 50%, while the fixing probability of the L_1 carrier phase ambiguity N_1 is about 30%. One reason for the lower fixed probability of N_1 is that the wavelength of L_1 is shorter and N_1 is more sensitive to measurement noise. Another reason is that the carrier phase ambiguity resolution is influenced by the convergence rate of the float solution.

3.2 Range error calibration

The range data of the TT&C system is generated based on the range error model. Considering the amplitude of the range error typical in space missions, in this study we assume $\Delta R_{g0}+R_{s0}=30$, $a_f=10^{-5}$, $a_{g0}+a_{s0}=100$, $a_{trop}=0.2$, $a_{ion}=10^8$, and range random error ε is modeled as Gaussian white noise with a 1.5 m standard deviation for the spread spectrum TT&C system or a 3 m standard deviation for the unified S-band TT&C system. Moreover, an analysis of the sensitivity to noise for the calibration procedure is described hereafter for different values of the random error. The range data of B1, B2, and B3 $R_{TT\&C,i,j}$ (i=1, 2, 3, j=1, 2) can be obtained from

$$\begin{aligned} R_{TT\&C,i,j} &= \rho + \Delta R_{BL,i,j} \\ &= \rho + 10^{-5}\rho + 30 + 100\Delta t + 100\Delta t \\ &\quad + R_{trop,model} + 0.2/\sin \mathrm{El}_r^{s_i} + R_{ion,model} \\ &\quad + 10^8 \times 5 \times 10^{-9}/\sin \mathrm{El}_r^{s_i} + \varepsilon_{BL,i,j}, \end{aligned} \tag{41}$$

where ρ is the geometrical distance from the ground station to the LEO. Subscript i=1, 2, 3 denotes the baseline number. Subscript j indicates the different value of the random error. When j=1, the standard deviation of the random error $\varepsilon_{\mathrm{BL},i,j}$ is 1.5 m; when j=2, the standard deviation of the random error $\varepsilon_{\mathrm{BL},i,j}$ is 3 m. $\Delta R_{\mathrm{BL},i,j}$ (i=1, 2, 3, j=1, 2) is the true range of error for the TT&C system.

Aimed at calibrating the systematic error of the range data, the DDGPS baseline solutions solved by the fixed-interval smoother are converted to the distance value $R_{\mathrm{GPS},i}$ (i=1, 2, 3). $R_{\mathrm{GPS},i}$ (i=1, 2, 3) is then used as a comparative reference to calibrate the range error of $R_{\mathrm{TT\&C},i,j}$. A batch LSQ algorithm is adopted to solve the range error model, which was described in detail in Section 2.

$$\varepsilon_{\mathrm{LSQ},i,j} = \Delta R_{\mathrm{LSQ},i,j} - \Delta R_{\mathrm{BL},i,j}. \tag{42}$$

As shown in Figs. 7–9, the range error expressed as $\Delta R_{\mathrm{LSQ},i,j}$ (i=1, 2, 3, j=1, 2) calibrated by the batch LSQ algorithm fits the variation of the range error $\Delta R_{\mathrm{BL},i,j}$ (i=1, 2, 3, j=1, 2) precisely. The bias $\varepsilon_{\mathrm{LSQ},i,j}$ (i=1, 2, 3, j=1, 2), which is formed according to Eq. (42), is quite consistent with the random error $\varepsilon_{\mathrm{BL},i,j}$. As shown in the lower half of these figures, the mean values of the bias $\varepsilon_{\mathrm{LSQ},i,j}$ are close to zero. Moreover, the difference between the standard deviations of $\varepsilon_{\mathrm{LSQ},i,j}$ and $\varepsilon_{\mathrm{BL},i,j}$ is less than 5 cm (Table 6). This indicates that $\Delta R_{\mathrm{LSQ},i,j}$ can be regarded as the systematic error of the range data.

Table 6 Standard deviation of the random error (m)

Baseline	Random error	Standard deviation	Residual error
B1	$\varepsilon_{\mathrm{LSQ},1,1}$	1.5367	0.0258
	$\varepsilon_{\mathrm{BL},1,1}$	1.5625	
	$\varepsilon_{\mathrm{LSQ},1,2}$	3.2038	0.0456
	$\varepsilon_{\mathrm{BL},1,2}$	3.2494	
B2	$\varepsilon_{\mathrm{LSQ},2,1}$	1.5650	0.0312
	$\varepsilon_{\mathrm{BL},2,1}$	1.5962	
	$\varepsilon_{\mathrm{LSQ},2,2}$	3.0512	0.0487
	$\varepsilon_{\mathrm{BL},2,2}$	3.0025	
B3	$\varepsilon_{\mathrm{LSQ},3,1}$	1.8584	0.0351
	$\varepsilon_{\mathrm{BL},3,1}$	1.8233	
	$\varepsilon_{\mathrm{LSQ},3,2}$	2.7264	0.0261
	$\varepsilon_{\mathrm{BL},3,2}$	2.7003	

As shown in Figs. 7–9, when the standard deviation of the random error $\varepsilon_{\mathrm{LSQ},i,j}$ is different, the error calibration results are shown in subfigures (a) and (b) respectively, and the corresponding statistical values of the residual errors are also given in Table 6. A comparison of subfigures (a) and (b) indicates that the online error calibration method is not sensitive to the change in random error.

The online error calibration results show that the online error calibration method can accurately separate the systematic error of the range data and thus the accuracy of the range data is affected only by the random error.

To better illustrate the benefits of online error calibration, the error calibration results of the traditional calibration method are also given here for comparison. As described in the introduction section, for traditional calibration, the TT&C measurement error needs to be calibrated before the launch of a new satellite. However, the residual error, which can be inspected by means of some auxiliary technologies, varies over time and becomes large during the period of on-orbit operation. Fig. 10 shows the data in the arc of Chinese ocean satellite tracked by a TT&C ground station. As can be seen in this figure, the mean of the residual range errors is up to 10 m. In contrast, the residual systematic errors of the online error calibration method are close to zero (Figs. 7–9). These results show the superiority of the new method over the traditional method.

In many application fields, robust fault detection and fault-tolerant control have received considerable attention in recent years (Li et al., 2010; Kommuri et al., 2016). Herein, the robustness of an online calibration method with regard to GPS receiver failures is considered. In the calibration satellite ZDPS-3, the following measures were used to guarantee the robustness of the new method. First, two spaceborne GPS receivers were equipped for backup. In addition, to prevent the anomaly of one channel, each spaceborne receiver had more than 24 channels to capture and track more GPS satellites. Furthermore, in the LEO-ground baseline determination algorithm, the outliers in the GPS observations were excluded by a threshold, and the gross errors of the GPS observations were processed by means of a weight reduction in the ARKF filter.

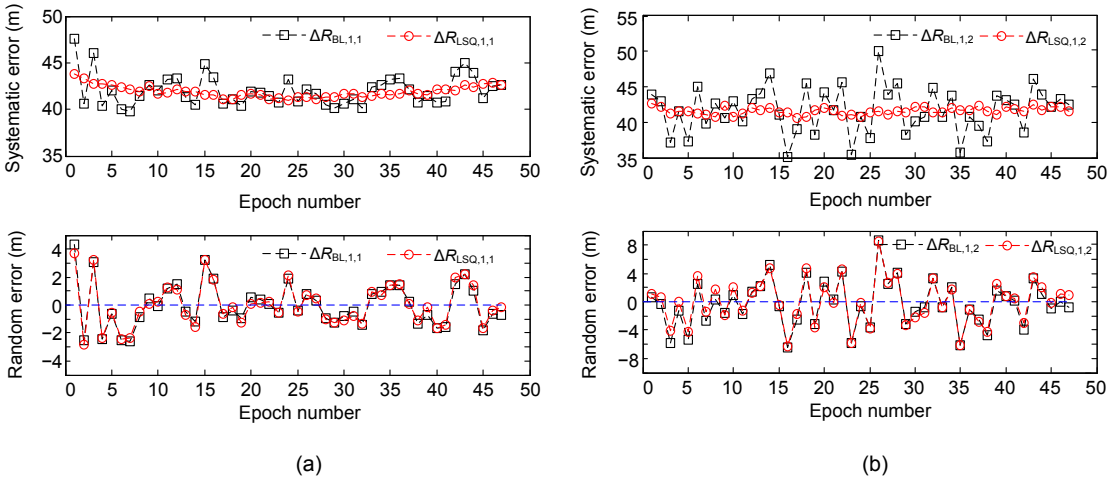

Fig. 7 Error calibration of B1: (a) $\varepsilon_{BL,1,1}$=1.5; (b) $\varepsilon_{BL,1,2}$=3

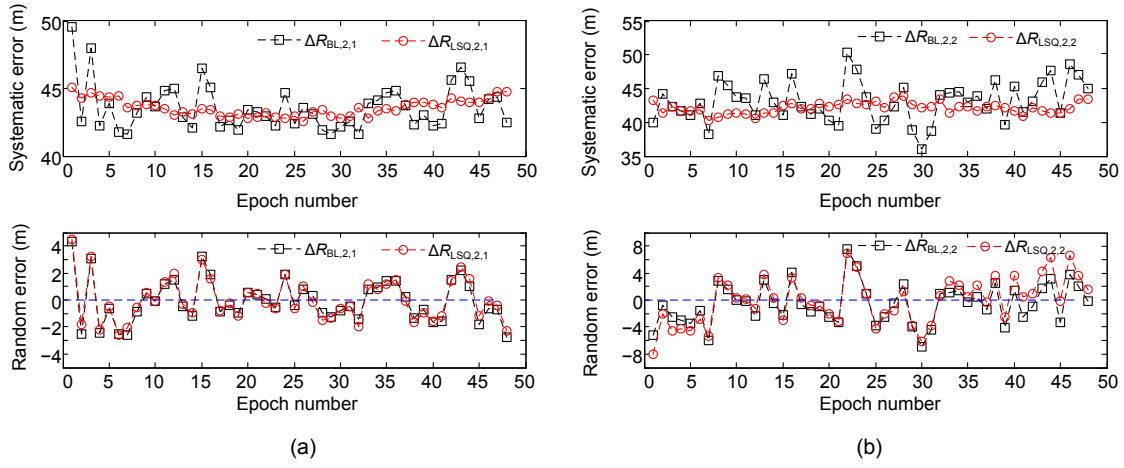

Fig. 8 Error calibration of B2: (a) $\varepsilon_{BL,2,1}$=1.5; (b) $\varepsilon_{BL,2,2}$=3

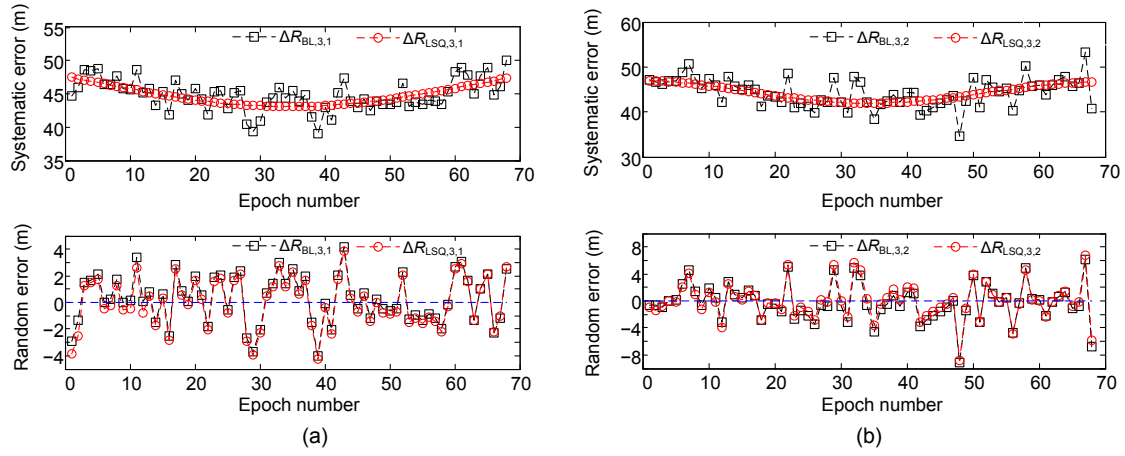

Fig. 9 Error calibration of B3: (a) $\varepsilon_{BL,3,1}$=1.5; (b) $\varepsilon_{BL,3,2}$=3

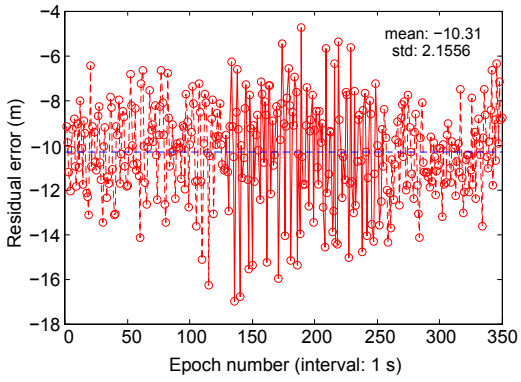

Fig. 10 Residual error of the traditional calibration method

4 Conclusions

To overcome the shortcomings of traditional calibration methods and ensure the measurement accuracy of spaceflight TT&C systems, an online error calibration method based on LEO-ground DDGPS was proposed in this paper. The traditional calibration methods, whether the tower calibration method or the aircraft calibration method, have a significant disadvantage in the inability to reflect the dynamic characteristics of an orbiting satellite, which has led to large residual TT&C measurement errors even after calibration. In comparison, the new online error calibration method can consistently provide a high precision baseline solution during on-orbit operation. Using this solution as the reference, the measurement error can always be accurately calibrated despite variations in systematic errors. Simulation results show that with the proposed method, a LEO-ground DDGPS baseline solution with an accuracy of better than 10 cm can be obtained, and the systematic error of range measurement can be accurately separated, which results in a residual systematic error of less than 5 cm. This indicates that the measurement error of TT&C systems is almost fully calibrated and thus affected only by the random error.

Future work will focus on the following aspects. First, accurate modeling of the TT&C measurement error will be investigated and studied according to the different error characteristics for various TT&C ground stations. Second, a combination of GPS and BeiDou navigation systems will be adopted to improve the LEO-ground baseline accuracy. Finally, actual calibration missions will be conducted to validate the performance of the new online error calibration method.

Compliance with ethics guidelines

Qiao WANG, Xiao-jun JIN, Wei ZHANG, Shi-ming MO, Zhao-bin XU, and Zhong-he JIN declare that they have no conflict of interest.

References

Blewitt G, 1989. Carrier phase ambiguity resolution for the Global Positioning System applied to geodetic baselines up to 2000 km. *J Geophys Res Sol Earth*, 94(B8): 10187-10203. https://doi.org/10.1029/JB094iB08p10187

Boehm J, Niell A, Tregoning P, et al., 2006. Global mapping function (GMF): a new empirical mapping function based on numerical weather model data. *Geophys Res Lett*, 33(7):L07304. https://doi.org/10.1029/2005GL025546

Box GEP, Muller ME, 1958. A note on the generation of random normal deviates. *Ann Math Stat*, 29(2):610-611. https://doi.org/10.1214/aoms/1177706645

Dorigo M, Maniezzo V, Colorni A, 1996. Ant system: optimization by a colony of cooperating agents. *IEEE Trans Syst Man Cybern*, 26(1):29-41. https://doi.org/10.1109/3477.484436

Gelb A, 1974. Applied Optimal Estimation. MIT Press, Cambridge, the UK.

Jazaeri S, Amiri-Simkooei AR, Sharifi MA, 2013. Fast GNSS ambiguity resolution by ant colony optimisation. *Surv Rev*, 45(330):190-196. https://doi.org/10.1179/1752270612Y.0000000010

Kommuri SK, Defoort M, Karimi HR, et al., 2016. A robust observer-based sensor fault-tolerant control for PMSM in electric vehicles. *IEEE Trans Ind Electron*, 63(12):7671-7681. https://doi.org/10.1109/TIE.2016.2590993

Langer JV, Feess WA, Hanington KM, et al., 1994. RADCAL: precision orbit determination with a commercial grade GPS receiver. Proc National Technical Meeting of the Institute of Navigation, p.421-431.

Li XB, Mo SF, Zhou KM, 2010. Fault detection for linear discrete time-varying systems. 49th IEEE Conf on Decision and Control, p.762-767. https://doi.org/10.1109/CDC.2010.5718034

Li ZS, Liu M, Karimi HR, et al., 2013. Sampled-data control of spacecraft rendezvous with discontinuous Lyapunov approach. *Math Probl Eng*, 2013:814271. https://doi.org/10.1155/2013/814271

Lin SG, 2015. Assisted adaptive extended Kalman filter for low-cost single-frequency GPS/SBAS kinematic positioning. *GPS Sol*, 19(2):215-223. https://doi.org/10.1007/s10291-014-0381-9

Liu DL, 2015. The Research on Methods and Key Technologies of Ship-Board Radar Detection Accuracy Calibration. PhD Thesis, Dalian Maritime University, Dalian (in Chinese).

Liu H, Nassar S, El-Sheimy N, 2010. Two-filter smoothing for accurate INS/GPS land-vehicle navigation in urban centers. *IEEE Trans Veh Technol*, 59(9):4256-4267. https://doi.org/10.1109/TVT.2010.2070850

Martin LK, Fisher NG, Jones WH, et al., 2011. Ho'oponopono: a radar calibration CubeSat. 25th Annual AIAA/USU Conf on Small Satellites.

Matias B, Oliveira H, Almeida J, et al., 2015. High-accuracy low-cost RTK-GPS for an unmanned surface vehicle. OCEANS-Genova, p.1-4. https://doi.org/10.1109/OCEANS-Genova.2015.7271673

Niell AE, 1996. Global mapping functions for the atmosphere delay at radio wavelengths. *J Geophys Res Sol Earth*, 101(B2):3227-3246. https://doi.org/10.1029/95JB03048

Reimann M, Doerner K, Hartl RF, 2004. D-ants: savings based ants divide and conquer the vehicle routing problem. *Comput Oper Res*, 31(4):563-591. https://doi.org/10.1016/S0305-0548(03)00014-5

Saastamoinen J, 1972. Atmospheric correction for troposphere and stratosphere in radio ranging of satellites. 3rd Int Symp on the Use of Artificial Satellites for Geodesy.

Socha K, Dorigo M, 2008. Ant colony optimization for continuous domains. *Eur J Oper Res*, 185(3):1155-1173. https://doi.org/10.1016/j.ejor.2006.06.046

Švehla D, Rothacher M, 2003. CHAMP double-difference kinematic POD with ambiguity resolution. In: Reigber C, Lühr H, Schwintzer P (Eds.), First CHAMP Mission Results for Gravity, Magnetic and Atmospheric Studies. Springer Berlin Heidelberg, p.70-77. https://doi.org/10.1007/978-3-540-38366-6_11

Takasu T, Yasuda A, 2008. Evaluation of RTK-GPS performance with low-cost single-frequency GPS receivers. Proc Int Symp on GPS/GNSS, p.852-861.

Takasu T, Yasuda A, 2009. Development of the low-cost RTK-GPS receiver with an open source program package RTKLIB. Int Symp on GPS/GNSS.

Teunissen P, Joosten P, Tiberius C, 2003. A comparison of TCAR, CIR and LAMBDA GNSS ambiguity resolution. Proc 15th Int Technical Meeting of the Satellite Division of the Institute of Navigation.

Teunissen PJG, de Jonge PJ, Tiberius CCJM, 1997. Performance of the LAMBDA method for fast GPS ambiguity resolution. *Navigation*, 44(3):373-383. https://doi.org/10.1002/j.2161-4296.1997.tb02355.x

Verhagen S, Li BF, Teunissen PJG, 2013. Ps-LAMBDA: ambiguity success rate evaluation software for interferometric applications. *Comput Geosci*, 54:361-376. https://doi.org/10.1016/j.cageo.2013.01.014

Wan N, Liu M, Karimi HR, 2014. Observer-based robust control for spacecraft rendezvous with thrust saturation. *Abstr Appl Anal*, 2014:710850. https://doi.org/10.1155/2014/710850

Xu GC, Xu Y, 2016. GPS: Theory, Algorithms and Applications (3rd Ed.). Springer, New York, USA.

Yang YX, Gao WG, 2006. An optimal adaptive Kalman filter. *J Geod*, 80(4):177-183. https://doi.org/10.1007/s00190-006-0041-0

Zhang HP, Ping JS, Zhu WY, et al., 2006. Brief review of the ionospheric delay models. *Progr Astron*, 24(1):16-26 (in Chinese). https://doi.org/10.3969/j.issn.1000-8349.2006.01.002